coasts

MDPI

Article

Quantifying Recent Storm-Induced Change on a Small Fetch-Limited Barrier Island along North Carolina's Crystal Coast Using Aerial Imagery and LiDAR

Hannah Sirianni [1,*], Matthew J. Sirianni [2], David J. Mallinson [2], Niels L. Lindquist [3], Lexia M. Valdes-Weaver [4], Michael Moody [1], Brian Henry [5], Christopher Colli [5], Brian Rubino [6], Manuel Merello Peñalver [5] and Carter Henne [5]

[1] Department of Geography, Planning & Environment, East Carolina University, Greenville, NC 27858, USA
[2] Department of Geological Sciences, East Carolina University, Greenville, NC 27858, USA
[3] Institute of Marine Sciences, University of North Carolina-Chapel Hill, Morehead City, NC 28557, USA
[4] North Carolina Coastal Federation, Newport, NC 28570, USA
[5] Sea & Shoreline, LLC., Winter Garden, FL 34778, USA
[6] Quible & Associates, P.C., Powells Point, NC 27966, USA
* Correspondence: siriannih21@ecu.edu

Abstract: Barrier islands within sheltered environments are an important natural defense from severe storm impacts for coastal communities worldwide. Despite their importance, these fetch-limited barrier islands remain understudied and their ability to withstand and recover from storms is not well-understood. Here, we present a case study of Sugarloaf Island in North Carolina that demonstrates the operational use of openly accessible LiDAR and aerial imagery data to quantify synoptic habitat, shoreline, and volumetric change between 2014 and 2020, a period that encompasses four hurricanes and a winter storm event. During this time period, our results show: (1) an 11–13% decrease in marsh and shrub habitat, (2) an average landward shoreline migration of 2.9 m yr^{-1} and up to 5.2 m yr^{-1} in extreme areas, and (3) a net volume loss of approximately 9800 m^3. The results of this study highlight the importance of storms as a driver of morphologic change on Sugarloaf Island and have implications for better understanding the resiliency of fetch-limited barrier islands to storms. This work helps to enhance prerestoration data availability and supports knowledge-based decision-making regarding habitat change, erosional issues, and the efficacy of nature-based solutions to increase the resiliency of a coastal community in North Carolina.

Keywords: barrier islands; fetch-limited; LiDAR; aerial imagery; storms; change detection; bio-geomorphology; remote sensing; nature-based solutions; coastal governance

Citation: Sirianni, H.; Sirianni, M.J.; Mallinson, D.J.; Lindquist, N.L.; Valdes-Weaver, L.M.; Moody, M.; Henry, B.; Colli, C.; Rubino, B.; Peñalver, M.M.; et al. Quantifying Recent Storm-Induced Change on a Small Fetch-Limited Barrier Island along North Carolina's Crystal Coast Using Aerial Imagery and LiDAR. *Coasts* **2022**, *2*, 302–322. https://doi.org/10.3390/coasts2040015

Academic Editor: Yannis Androulidakis

Received: 17 September 2022
Accepted: 25 October 2022
Published: 14 November 2022

1. Introduction

Barrier islands are highly dynamic coastal landforms that provide storm defenses for roughly 10% of the world's open-ocean coastlines, particularly in the U.S., where 24% of the world's barrier islands occur [1]. While open-ocean-facing barrier island evolution has been subject to intense scientific study for nearly 180 years (e.g., [2–18]), barrier islands that form within sheltered and fetch-limited environments such as bays, lagoons, and sounds have received little attention or systematic research. In fact, they were an unrecognized coastal landform until recently [14,15]. Termed fetch-limited barrier islands (hereinto fetch-limited islands), these islands are about six times more numerous than open-ocean-facing barrier islands and, often, front estuarine shorelines with sensitive community development [15–21]. As such, fetch-limited islands serve as important barriers for coastal communities that buffer them against intense wave action and other storm event impacts [22,23]. By the end of the century, coastal issues are anticipated to have worsened as a result of spatiotemporally variable accelerated sea-level rise (e.g., [24]),

elevated storm frequency and intensity (e.g., [25]), and increased coastal development (e.g., [20]). Barrier islands will be particularly vulnerable to these factors, considering that a 50% acceleration in barrier island retreat is expected due to a lagged response to previous sea-level rise [26]. It is therefore critical to better understand the spatiotemporal resiliency of fetch-limited islands to storms, particularly where coastal communities rely on them as nature-based coastal defense infrastructure.

Fetch-limited islands have a complex evolutionary dynamic with storms. Intense and/or prolonged coastal storms can subject islands to elevated water levels, wave runup, and/or wave attack that exceed the island's ability to withstand prolonged erosion, thereby causing them to disappear entirely [1,14]. Yet overwash, the storm-driven process where sediments eroded from the beach and foredune are carried inland and deposited into back barrier marsh environments, is typically the most important sediment transport process responsible for fetch-limited island evolution [15]. During nonstorm conditions, fetch-limited island morphology is predominately influenced by low-energy, locally generated waves and negligible aeolian inputs [15,21,27,28]. As a result, fetch-limited island systems are thought to show little change during poststorm recovery periods, making their morphology a product of storm events [15,21,27,28]. In comparison, during nonstorm conditions, open-ocean-facing barrier systems can be exposed to higher-energy, nonlocally generated waves, such as those from further offshore or other ocean basins [21,27,28]. As a result, open-ocean-facing barrier systems can experience cyclical poststorm recovery patterns, where mobilized offshore bars are transported landward and provide a sediment source for features such as dunes to reform following damage from storm events [15,27–32]. Fetch-limited islands are thus particularly vulnerable to high-energy coastal storms if they do not experience a poststorm recovery period like open-ocean barrier systems. However, recent work (e.g., [21]) on inlet barrier islands (a subgroup of fetch-limited islands studied by [15]) in North Carolina suggests that over time, some fetch-limited islands may fall into and out of conformance with the open-ocean-facing barrier system poststorm recovery model. Considering the lack of studies and lack of agreement between studies in the available literature, it is important to better understand and monitor the spatiotemporal resiliency of fetch-limited islands to storm events.

Storm impacts on barrier islands are primarily a function of the combined effects of storm-induced water levels, wave energy, storm duration, island morphology, and the island's resiliency to prolonged erosion [33,34]. However, other variables such as storm path, storm timing, and vegetation cover can also affect coastal responses to storms [35]. This relationship is conceptualized in the Sallenger Storm Impact Scale by four storm impact regimes with increasing magnitudes of potential hazards [33]. These four regimes are defined as swash, collision, overwash, and inundation. The swash regime is the lowest impact level and defined where wave runup is confined to the foreshore and where no net change occurs [33]. The next impact level is the collision regime where wave runup exceeds the base of the foredune ridge or berm and results in net dune erosion [33]. The overwash regime is the third highest impact level and is defined where wave runup overtops the foredune ridge or berm and results in net landward sediment transport and net landward migration of the barrier island [33]. Lastly, the highest impact regime is the inundation regime where water level only is sufficient to continually submerge the barrier island, resulting in net landward sediment transport over the barrier island in quantities and distances greater than what occurs during overwash regime impacts [33]. The Sallenger Storm Impact Scale can be used to reasonably predict the coastal response to storms and explain aspects of the spatial variability observed related to shoreline and volumetric change magnitude [36]. Since many fetch-limited islands are typically uninhabited and unmonitored, quantitative historical information regarding their morphological change is not readily available and may only be anecdotal in nature, if it exists at all [15]. Openly available (e.g., NOAA's Data Access Viewer) remote sensing datasets, such as Light Detection and Ranging (LiDAR) and aerial imagery, therefore play a critical role in providing

accurate and reliable data for synthesizing historical change estimates and monitoring ongoing changes in complex coastal environments [15,37–41].

Here we present a case study that demonstrates the operational use of remote sensing technologies to support knowledge-based management of coastal resources. The main objectives of this study are two-fold: (1) to further understand the influence of storms on the bio-geomorphology of fetch-limited islands, and (2) to synthesize a remotely sensed knowledge base for an ongoing coastal restoration project. Specifically, we use openly accessible LiDAR and aerial imagery data to quantify synoptic habitat, shoreline, and volumetric change on a fetch-limited island in central eastern North Carolina between 2014 and 2020, a period that encompasses four hurricanes and a winter storm event. This work is unique and timely in that it (1) enhances understanding of the relationship between coastal processes and the bio-geomorphology of fetch-limited islands, (2) contributes to a larger multidisciplinary coastal governance project that combines efforts from private citizens, governmental and nongovernmental organizations, and academia, and (3) enhances prerestoration data availability that supports knowledge-based decision-making regarding habitat change, erosional issues, and the efficacy of innovative science- and nature-based solutions to increase the resiliency of fetch-limited islands.

2. Site Description and Historical Context

The North Carolina coastal region comprises of ~23 open-ocean-facing barrier islands that cover ~320 km of shoreline, as well as over 4800 km of estuarine shoreline comprising coastal communities, back barrier marsh, and oyster-reef habitats known as the Inner Banks [42,43]. Sugarloaf Island is a small, anthropogenically modified fetch-limited barrier island (~14 ha) located in Morehead City, North Carolina, within a region called the 'Crystal Coast' (indicated by the red dot and green outline in Figure 1A). Sugarloaf Island is situated landward of the developed open-ocean-facing barrier island, Bogue Banks, in the eastern end of the Bogue Sound near its confluence with the Beaufort Inlet Channel that connects the Sound with the Atlantic Ocean (Figure 1B). As early as 1888, modern Sugarloaf Island was identified on nautical charts as a marsh island [44]. By 1913, the Island is shown to have developed some subaerial exposure [45], which is likely due to dredge-spoil deposition associated with the construction of an anchorage basin along Morehead City's waterfront between 1910 and 1913 [46]. Dredge-spoil deposition would continue to augment islands in this area throughout the 20th century. A portion of Sugarloaf Island was modified from spoils associated with Port of Morehead City navigational improvements along the city's waterfront in the 1950's [46–48]. However, no additional spoil deposition on the Island has been documented by the Army Corps of Engineers for at least the past 35 years [48], and the island has characteristics of a natural fetch-limited barrier island.

Contemporarily, Sugarloaf Island is bounded on the north and east sides by the Harbor Channel, separating the Island by approximately 100 m from the city's commercial downtown waterfront and port areas. The western end of the Island is characterized by a recurved sandy spit (i.e., West Spit in Figure 1C) that partially encloses a shallow back-barrier lagoon and marsh along its northern-facing shoreline (i.e., Back Barrier Marsh in Figure 1C). Moving to the east, the south-facing shoreline transitions to a rapidly eroding sediment bank escarpment with dense woody vegetation (e.g., *Morella cerifera* (wax myrtle)). Past the sediment bank to the east (i.e., East Spit in Figure 1C), the Island is again characterized by a sandy barrier ridge and spit with washover deposits and a back barrier marsh dominated by *Spartina alterniflora* (smooth cordgrass). Within the back barrier marsh, there are two tidal creeks that can segment the Island into three smaller islands during elevated water levels. During higher-than-normal tides and storm conditions, this area can experience overwash, as is evidenced by the presence of washover deposits. The south- and southeast-facing shorelines along the East Spit are characterized by a thin sandy shoreface with scattered patches of beach and dune grasses (e.g., *Spartina patens* (salt meadow cordgrass)). On both the West and East Spit areas, previously buried marsh

deposits are exposed along the shoreline and are actively eroding away. Examples of the different habitat types on Sugarloaf Island are shown in Figure 1D. Sugarloaf Island experiences semidiurnal tides with a mean tidal range of 0.9 m (Beaufort, Duke Marine Lab, NC—Station ID: 8656483). Sugarloaf Island's proximity to and parallel orientation with the city's waterfront area provides the community with protection during marine weather events and is critical to Morehead City's future resiliency.

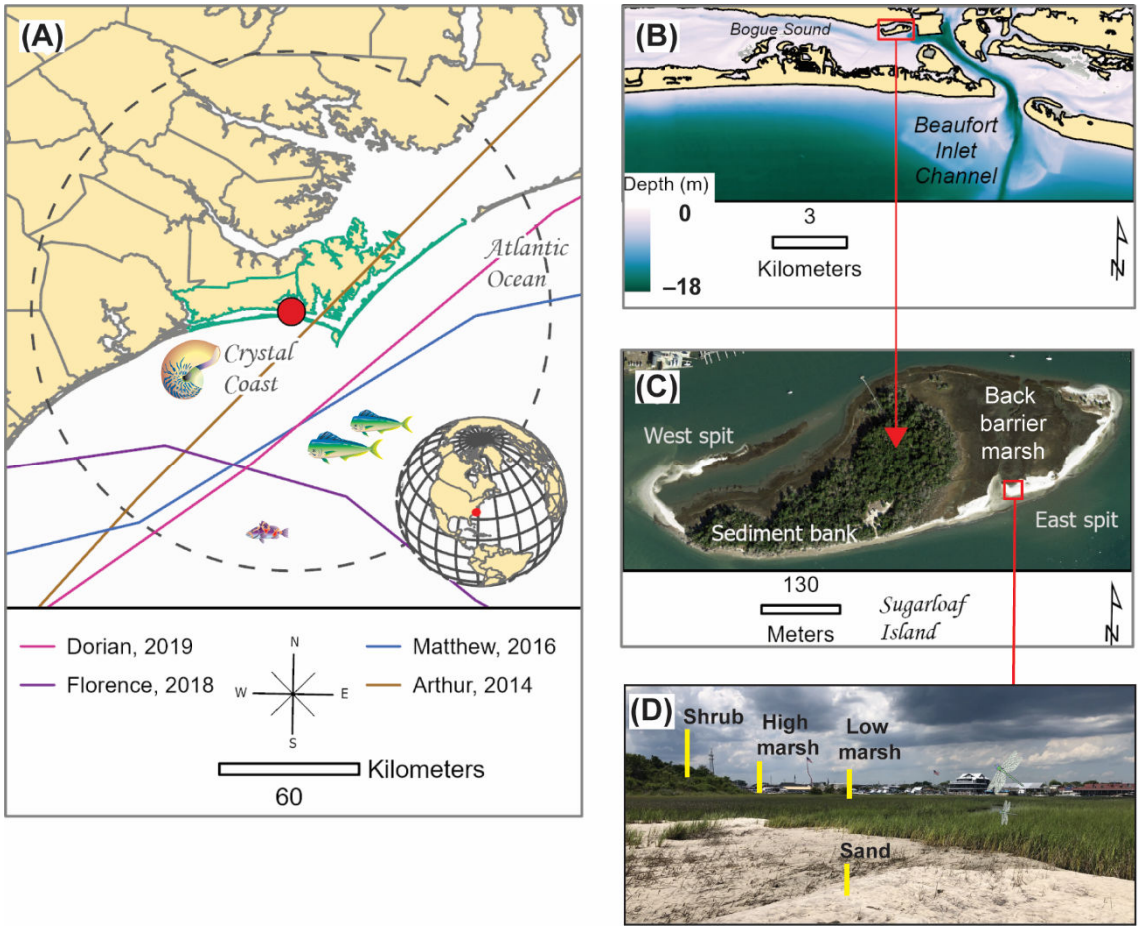

Figure 1. Maps of different scales of Sugarloaf Island located in North Carolina's Crystal Coastal region. (**A**) The location of Sugarloaf Island is indicated by a red dot. The dotted circle denotes a 60 nautical mile radius from the Island where hurricanes passed. Hurricane-best-track data obtained from: https://www.nhc.noaa.gov/data/ (accessed on 25 October 2022), (**B**) 2010 bathymetry model from TCarta Marine LLC, (**C**) RGB aerial imagery from 2020, (**D**) visual line of sight captured while in the field in June 2022.

Anecdotally, the seaward shoreline of Sugarloaf Island experiences shoreline erosion from wave exposure and currents that destroy vegetation and sweep sediment from the Island into the water, thereby contributing to nearby navigational channel infilling and water quality deterioration. This trend is shown in historical satellite imagery from 1984 to 2020, which shows the island contracting in the north, east, and west directions with no visually noticeable recovery year over year [49]. Moreover, local reports document striking and accelerating morphologic and ecologic changes to Sugarloaf Island in association with storms; however, to the authors' knowledge, the Island has never been formally studied and historical changes are poorly documented. In an effort to increase the resiliency of downtown Morehead City, a partnership consisting of private citizens, governmental and nongovernmental organizations, and academia was created to protect Sugarloaf Island from continued erosion by implementing nature-based stabilization methods. These methods include: (1) wave attenuation devices to reduce erosion, (2) aquatic and

terrestrial plantings to stabilize sediment and create habitat, and (3) living shorelines to build saltmarsh and upland vegetation. In recognition of the economic importance of this island as a tourist destination and coastal defense resource, the project was awarded USD 2 million by the North Carolina General Assembly in the state's 2022 budget. To support the implementation of this project, remote sensing techniques were used to enhance Sugarloaf Island's prerestoration data availability in order to (1) better understand recent habitat, shoreline, and volumetric change in relation to storm events and (2) establish a baseline dataset by which the efficacy of future restoration activities can be assessed.

3. Data and Methods

3.1. Data Availability and Description

At the time of this study, the best available openly accessible topobathymetric LiDAR and corresponding aerial imagery were from 2014 and 2020 and are available through NOAA's Data Access Viewer (https://coast.noaa.gov/dataviewer/; accessed on 25 October 2022). Both the 2014 and 2020 topobathymetric LiDAR were collected between the months of November and April, while the 2014 and 2020 aerial imagery were collected between the months of January and April. All datasets are horizontally referenced to the North American Datum of 1983 (NAD 83) and projected to the State Plane Coordinate System in meters. Additional aerial imagery were available, but corresponding LiDAR collected during the same year and season were not. Since wetland plant productivity and growth is sensitive to small variations in elevation on the order of centimeters [50], LiDAR elevation is an important feature when driving a machine learning algorithm to classify habitat [51]. For these reasons, the authors limited the study to the 2014 and 2020 datasets.

The 2014 and 2020 topobathymetric LiDAR were acquired using Riegle VQ sensors and then classified as ground and submerged topography classes before the vendor generated 1 m horizontal resolution topobathymetric LiDAR DEMs. The vertical accuracy of each DEM was assessed by each vendor using independent survey checkpoints. The reported open terrain vertical Root Mean Square Error (RMSE) was 0.057 m for the 2014 DEM and 0.037 m for the 2020 DEM [52,53]. The 2014 and 2020 DEMs were vertically referenced to the North American Vertical Datum of 1988 (NAVD 88) using Geoid 12B. In this study, we converted the DEMs to local tidal datums of Mean Lower Low Water (MLLW) and Mean Higher High Water (MHHW) using NOAA's open-source vertical datum transformation tool, VDatum (https://vdatum.noaa.gov/; accessed on 25 October 2022). MLLW represents the modern lowest low-water mark, which allows us to identify where land is dry daily. On the other hand, MHHW is the modern highest high-water mark, and is used in this study as a baseline to capture areas inundated by storms. The maximum cumulative uncertainty, which is the value from the transformation from the International Terrestrial References Frame to a tidal datum, is 0.09 m for the North Carolina coastal region (https://vdatum.noaa.gov/; accessed on 25 October 2022).

The 2014 aerial imagery was acquired with an Intergraph/Leica DMC sensor at a 0.35 m ground sampling distance and horizontal accuracy tested at 0.53 m [54]. The specifications for the 2020 aerial imagery included data acquisition with a Leica ADS100 pushbroom sensor, a slightly better ground sampling distance of 0.3 m, and horizontal accuracy of 0.28 m [55]. Both the 2014 and 2020 imagery contained 4 bands (i.e., Red (R), Green (G), Blue (B), and Near-Infrared (NIR)), but were not tidally controlled. Therefore, we performed a quality assessment in a GIS by overlaying the transparent imagery with the respective DEM relative to MLLW to determine any potentially submerged areas that were dry at low tide [56]. The results showed that the 2014 imagery was collected at low tide, while the 2020 imagery was collected near low tide. Since the images were collected at similar tidal stages, they were considered suitable for further analysis as recommended by other previous studies [56–61].

3.2. Image Analysis and Classification Workflow

In this study, we use a well-established workflow to segment and classify aerial imagery using object-based image analysis (OBIA) and the Random Forest (RF) machine learning algorithm. OBIA is a technique used to recognize homogeneous objects in digital imagery through image segmentation and classification [62]. The defined objects can have varying shapes and sizes and can also incorporate spectral, textural, and contextual statistics associated with them to classify objects. RF is an ensemble classification technique, developed by [63], that can be used to predict image classes based on the partition of data from multiple uncorrelated decision trees. Advantages of RF include its speed, capability to deal with complex relationships between predictors, ease of input parameter specification, and accuracy of its classifications compared to other machine learning models [64,65].

This study used an OBIA workflow in Esri's ArcGIS Pro v2.9.3, which consisted of the following three main steps. In the first step of the OBIA workflow, the Segment Mean Shift algorithm uses a moving window average to group pixels with similar spectral characteristics into segments [66]. In the algorithm, there are three adjustable parameters: (1) spectral detail, (2) spatial detail, and (3) minimum segment size. The spectral detail and spatial detail parameters set the level of importance given to the spectral difference and the proximity between features, respectively. Both parameters range from 1 to 20, with higher numbers signifying greater sensitivity to slight differences between features. The minimum segment size parameter is directly related to the minimum mapping unit (i.e., the smallest size that can be used to capture a feature), and segments smaller than the minimum segment size are merged by the algorithm with their best-fitting neighbor segment. In this study, a spectral detail of 17, spatial detail of 15, and minimum segment size of 20 were used as inputs in the Segment Mean Shift algorithm.

The second step in the OBIA workflow involved the use of tools within Esri's Training Samples Manager to create representative class categories and training samples for each class and imagery date. Commonly, real-time kinematic global navigation satellite system (RTK-GNSS) data of each class type are collected at the time of imagery acquisition to aid in training. However, since no ancillary RTK-GNSS data were available for this study, training sample objects were created for each class category and imagery year through a supervised image classification scheme and a priori knowledge of the habitat types on the island over the past several years. Class categories were based on four major habitat types on the island: (1) high marsh, (2) low marsh, (3) sand, and (4) shrub (i.e., those shown in Figure 1D). High and low marsh were differentiated by a combination of RGB and false-color aerial imagery, DEMs relative to MHHW and MLLW, and a priori field observations (e.g., Figure 1D). A total of 1272 training sample objects were selected for the 2014 imagery and 952 for the 2020 imagery.

The last step in the OBIA workflow used Esri's Compute Segment Attributes tool to extract analytical information for each segment within the image. In this study, six explanatory variables were extracted and included: (1) LiDAR elevation minimum, (2) LiDAR elevation mean, (3) RGB band mean, (4) NIR band mean, (5) segment compactness (the degree to which a segment is compact or circular), and (6) segment rectangularity (the degree to which the segment is rectangular). The derived analytical information from each image was then synthesized into object layers and used as an input into the RF classification algorithm.

Esri's adaptation of the RF supervised classification algorithm, called Forest-based Classification and Regression (Spatial Statistic Tools), can be used to train the models before making predictions on unseen data. Training samples are randomly split into two datasets used to: (1) train and fine-tune the model's parameters used to classify the objects (80% of the training samples) and (2) test the predictive performance of the model used to generate the habitat maps (20% of the training samples). Based on trial and error, we used 500 trees in a forest where each tree included every one of the four habitat classes, a maximum tree depth that was data driven (set on the 500 trees and six explanatory variables),

and the number of randomly sampled explanatory variables used to create each decision tree was set to two. For each year, a total of 25 model runs were carried out to determine the most stable model based on the highest R^2 value. To help reduce overfitting, training time, and improve model accuracy, an automatic attribute selection was used for determining the relevant explanatory variables. The variables of importance identified for both imagery datasets included the LiDAR mean and minimum elevation as well as the RGB and NIR mean values. Once the models were trained, all training samples were used to make predictions on unseen data that were used to generate habitat maps.

3.3. Habitat, Shoreline, and Volumetric Change Detection

Changes in habitat were determined by calculating the total area for each habitat class category and calculating the percent difference between the 2014 and 2020 imagery. By analyzing various accuracy and error metrics of the classified maps, we can assess their suitability for understanding the relative composition of the major habitat types on the Island between 2014 and 2020. The validation of the model's performance is based on randomly selected independent test sample objects used to calculate the overall accuracy and kappa value. The overall accuracy provides information on what proportion of the test sites were correctly classified. On the other hand, the kappa value evaluates how well the classification performed when compared to randomly assigned classifications, with values close to 1 indicating classifications are better than random. Classification accuracies can also be examined from the map user and producer points of view. The user accuracy represents the probability that an object classified as a known class on the map represents that class on the true ground. On the other hand, the producer's accuracy represents how well the training sample objects of the ground class features are classified on the map. All these accuracy statistics were used in this study to assess the suitability of the classifications.

The shoreline is generally defined as the physical interface of land and water [66], yet this definition is challenging to objectively apply due to the dynamic water levels at the coastal boundary [56]. As such, numerous shoreline indicators have been used in the literature to define shoreline change through time (for a review see [56]). In this study, the shoreline was determined through a tidal datum-based indicator rather than a visually discernable feature-based indicator in order to increase objectiveness of our shoreline definition [56,67]. Specifically, we used the MLLW tidal datum to define the land–water boundary [68,69] in order to minimize tidal variation between years [70]. Changes in shoreline were calculated using a common endpoint method, where shoreline rate of change is equal to the change in horizontal shoreline position divided by the change in time between the two shorelines [70–72], with positive values indicating accretion and negative values indicating erosion. We calculated shoreline change rates at shore-normal transects spaced 5 m along the shoreline. The 2014 and 2020 horizontal shoreline positions from each transect were then used to calculate an annual rate of change. Consistent with NOAA's Coastal Mapping Program standards, where imagery must meet a 1.5 m horizontal accuracy at the 95% circular error confidence interval, we chose to remove all shoreline positions with differences in horizontal distance less than 1.5 m [53,54]. This was our minimum critical threshold for determining horizontal changes.

Morphological changes were quantified using the DEM of Difference (DoD) approach, a common method used in various morphological change-detection studies [73–75]. In this study, we applied the DoD approach to the 2014 DEM and 2020 DEM to quantify volumetric change. Since ground truth measurements were not available to estimate spatially variable DEM error [73], we subjected the spatially uniform DEM error to the Linear Error (LE) at a 95% confidence interval (RMSE × 1.96 = LE) [76] using the DEM with the highest error, which, in our case, was the 2014 DEM (RMSE = 0.057 m). In this study, the LE of ±0.11 m (0.057 × 1.96 = 0.11 m) was used as the minimum critical threshold for determining vertical changes. We chose to remove all DoD grid cells within the LE of ±0.11 m. The remaining DoD grid cells were then used to estimate erosion (negative values) and

deposition (positive values) volumes and create a volumetric difference map and histogram showing the distribution of elevation change across the Island. Given the synoptic nature of this study, we use the Sallenger Storm Impact Scale to understand the cumulative effect of storms on Sugarloaf Island's morphology and landscape composition between 2014 and 2020. This was performed by examining hourly wind speed, wind direction, and water level observations from a nearby (~2 km) tide station (Beaufort, Duke Marine Lab, NC—Station ID: 8656483) for each storm and topographic profiles extracted from each DEM to infer impacted regions across the Island.

4. Results

4.1. Habitat Change and Model Validation

Maps showing the total habitat distribution for the 2014 and 2020 imagery are shown in Figure 2A,B, respectively, with a table summarizing the important statistics below in Figure 2C. Overall, between 2014 and 2020, high marsh and shrub habitat experienced the largest percent change, both decreasing by 12.7% between 2014 and 2020. The low marsh habitat also experienced a decrease during this period, losing 11.8% of its 2014 area. In contrast to the other habitat types, the area predominantly characterized by sand increased by 1.2% between 2014 and 2020. Another noticeable difference between the habitat maps is the change in the shape of the Island, particularly the sand spits located on the eastern and western ends. This difference is highlighted by superimposing a black solid line parallel to the eastern and western extents of the 2014 Island in Figure 2A,B.

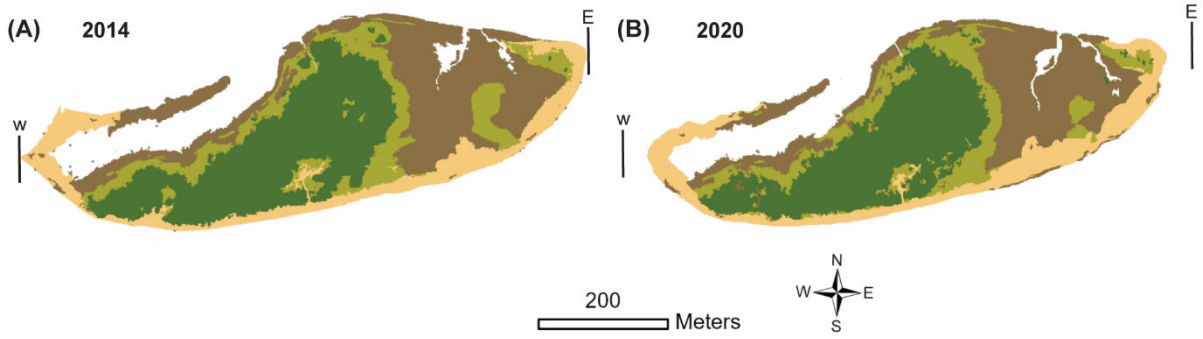

(C)

Habitat	2014 area (ha)	2020 area (ha)	Change (ha)
High marsh	2.8	2.4	−0.4
Low marsh	5.1	4.5	−0.6
Sand	2.5	2.5	*0.0
Shrub	5.5	4.8	−0.7
Total	15.9	14.2	−1.7

Asterisk * denotes change of 0.01 ha.

Figure 2. (**A**) 2014 habitat map, (**B**) 2020 habitat map, and (**C**) table showing the percentage of habitat decrease from 2014 to 2020. In the habitat maps, a color scheme was chosen where high marsh was assigned olive green, low marsh was leather brown, sand was medium sand, and shrub was spruce green.

As shown in Table 1, the overall accuracy of the 2014 and 2020 imagery classification is similar, with values of 0.921 and 0.903, respectively. Based on the minimum overall accuracy criteria of 0.85 set by the U.S. Geological Survey [77], these classifications are acceptable. Additionally shown in Table 1 are the kappa values for the 2014 and 2020 imagery classification. Like the overall accuracy results, the kappa values between the 2014 and 2020 classification are also similar, with values of 0.895 and 0.876, respectively.

Table 1. Classification accuracies for 2014 and 2020 of Sugarloaf Island.

Imagery Date	Overall Accuracy	Kappa Value
2014	0.921	0.895
2020	0.903	0.876

A summary of the user and producer accuracies per-class for the 2014 and 2020 habitat classification is shown in Table 2. For the 2014 imagery classification, the results show that the user and producer accuracies are the same for the high marsh and shrub classes. In contrast, the user accuracy for the low marsh class is less than the producer accuracy, while the user accuracy for the sand class is greater than the producer accuracy. For the 2020 imagery classification, no classes had the same user and producer accuracies. In contrast to the 2014 imagery, the high marsh, low marsh, and sand classes have a user accuracy that is less than the producer accuracy, while the shrub class has a greater user than producer accuracy. Overall, all user and producer accuracies are greater than or equal to 0.75, and the 2014 and 2020 imagery classifications were considered suitable, particularly when considering all accuracy statistics that were assessed.

Table 2. Per-class accuracy for habitat classification of Sugarloaf Island. Where UA = User's Accuracy and PA = Producer's Accuracy.

Classes	2014 Imagery		2020 Imagery	
	UA	PA	UA	PA
High Marsh	0.866	0.866	0.750	0.857
Low Marsh	0.937	1.000	0.818	0.900
Sand	1.000	0.750	0.882	0.937
Shrub	0.960	0.960	1.000	0.823

4.2. Shoreline Change

A more detailed map of the changes to the Island's shoreline is shown in Figure 3. Between 2014 and 2020, the Island decreased in area by 1.7 ha from 15.9 ha in 2014 to 14.2 ha in 2020. Like the habitat change maps, the shoreline change map in Figure 3 shows marked changes particularly on the eastern and western ends of the Island. Overall, the shoreline migrated landward between 2014 and 2020 by 2.9 m yr^{-1} on average and up to 5.2 m yr^{-1} in extreme areas such as the western end of the island. Another area of noticeable change is related to the tidal creeks in the northeastern portion of the Island. In both cases, the tidal creeks are observed to elongate toward the south–southeast and become more incised in the landscape. In general, the shoreline on the northern side of the island showed little to no change in position over the study period.

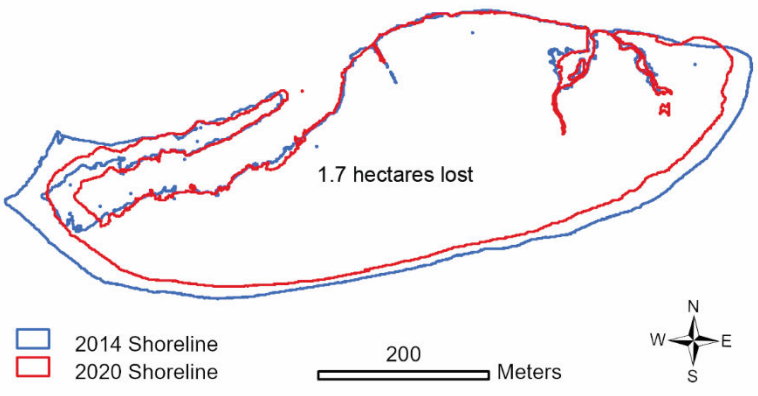

Figure 3. Shorelines derived from object-based image analysis techniques, where blue indicates 2014 and red indicates 2020.

4.3. Volumetric Change

The DEMs generated from the 2014 and 2020 LiDAR data relative to MHHW are shown in Figure 4A,B, respectively. Here, shades of blue indicate where beach and low marsh habitat are inundated at higher high tide, while shades of green and brown indicate areas with higher elevation such as high marsh and shrub habitat. Based on a qualitative inspection of the DEMs, there are several areas on the Island that have had noticeable volumetric change and are highlighted in Figure 4A,B by colored arrows. Highlighted by the red arrow in Figure 4A,B, we see that in 2014, there was a small breach in the narrow foredune just to the southeast of the tidal channel, but in 2020, the dune area above MHHW had grown more robust in width and height, and the breach had been filled. To the west and highlighted by the black arrow, we see a narrow foredune exposed just above MHHW in 2014, but in 2020, overwash had created a channel cutting through the narrow foredune.

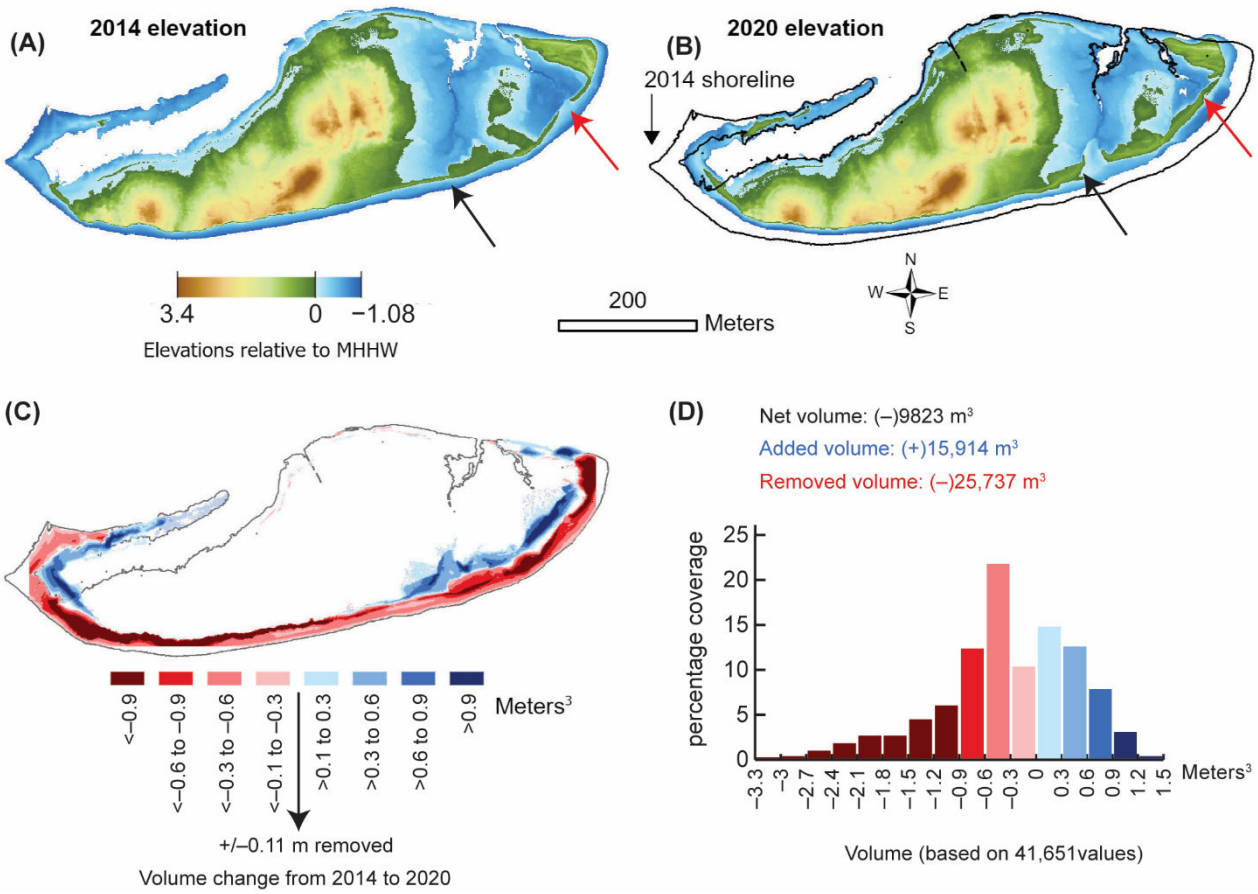

Figure 4. (**A**) 2014 DEM relative to Mean Higher High Water (MHHW); (**B**) 2020 DEM relative to MHHW, (**C**) difference of DEMs (DoD's) where the 2014 DEM was subtracted from the 2020 DEM and spatially uniform DEM error removed (+/−0.11 m) to reveal morphological change as erosion (red negative values) and deposition (blue positive values), and (**D**) corresponding bar graph showing elevation change distributions. Colored arrows in (**A**,**B**) depict features described in the text.

To provide a quantitative assessment of volumetric change as erosion and deposition, the differences between the 2020 and 2014 DEMs relative to MHHW were calculated, as shown in Figure 4 by the map (Figure 4C) and histogram (Figure 4D). Erosion is shown in red as negative values, while deposition is shown in blue as positive values. Overall, between 2014 and 2020, the Island experienced a net volume loss of approximately 9823 m³. There are three distinct erosional patterns shown in Figure 4: (1) very little to no change, (2) erosion without inland deposition, and (3) erosion with inland deposition. In

general, on the northern side of the Island, there is very little volumetric change detected between 2014 and 2020, with some stretches in this area experiencing no detectable volumetric change. In contrast, areas generally oriented to the south and associated with the sediment bank experienced moderate to high erosion without landward deposition, while areas generally oriented southwest or southeast experienced moderate to high erosion with landward deposition. Of the area that experienced detectable change between 2014 and 2020, approximately 61.8% experienced volumetric loss, while approximately 38.2% experienced volumetric gain. A histogram summarizing the distribution of volumetric change within the area that experienced detectable change between 2014 and 2020 is shown in Figure 4D.

4.4. Storm Characteristics

A summary of the wind and water level characteristics of the storm events that impacted Sugarloaf Island between 2014 and 2020 are shown in Table 3 in chronological order. For this study, a storm was considered to be any 24 h period where at least 1 h of tropical storm force winds (i.e., >17.4 m s^{-1}) impacted Sugarloaf Island. Over the course of the study, Sugarloaf Island received a total of approximately 22 h of tropical storm force winds over four hurricane events and one winter storm event. On average, Sugarloaf Island experiences gentle breeze conditions from the southeast with an average hourly wind speed of 3.7 m s^{-1}. Additionally, on average, the Island experiences approximately 0.14 m of inundation above MHHW for 3 h per day. Generally, the storms fall into two categories: (1) winds predominately from the west to southwest (e.g., Arthur, Matthew, Winter Storm, and Dorian) and (2) winds predominately from the east to southeast (e.g., Florence). Of all storms, Hurricane Florence reported the highest maximum and average wind speeds (i.e., 24.1 and 18.3 m s^{-1}, respectively), duration of tropical storm force winds (i.e., 13 h), maximum water level above MHHW (i.e., 1.12 m), duration of water level above MHHW (i.e., 23 h), and magnitude of average water level above MHHW (i.e., 0.50 m). Next, Hurricane Matthew and Dorian reported similar maximum and average wind speeds (i.e., 20.0 and 10.5 m s^{-1} and 19.6 and 10.6 m s^{-1}, respectively), duration of tropical storm force winds (i.e., 3 h), and duration of water levels above MHHW (i.e., 11 and 10 h, respectively). However, Hurricane Matthew reported higher maximum water levels (i.e., 0.64 m) and magnitude of average water level above MHHW (i.e., 0.28 m) than Hurricane Dorian (i.e., 0.41 and 0.23 m, respectively). Lastly, Hurricane Arthur and Winter Storm report similar maximum and average wind speeds (i.e., 20.3 and 6.5 m s^{-1} and 17.5 and 9.9 m s^{-1}, respectively) and duration of tropical storm force winds (i.e., 2 and 1 h, respectively). However, Winter Storm reports higher maximum water level above MHHW (i.e., 0.49 m), duration of water levels above MHHW (i.e., 6 h), and magnitude of average water level above MHHW (i.e., 0.28 m) than Hurricane Arthur (i.e., 0.42 m, 4 h, and 0.17 m, respectively).

Table 3. Summary of wind and water level characteristics of storm events that impacted Sugarloaf Island, NC, between 2014 and 2020. Note that maximum hourly wind speed is reported outside of parentheses, and average hourly wind speed is reported inside parentheses. Wind and water level duration are reported in hours (h). Duration of water level >MHHW for the total study period is reported in hours per day (h d^{-1}) and is highlighted by the asterisk.

Name	Date Near Sugarloaf Island	Hourly Wind Speed (m s^{-1}) Max (Avg.)	Duration of Tropical Winds >17.4 m s^{-1}	Avg Hourly Wind Direction	Max Hourly Water Level >MHHW (m)	Duration of Water Level >MHHW	Avg Magnitude of Water Level >MHHW (m)
Total Study Period		24.1 (3.7)	22 h	169°	1.12	3 h d^{-1}*	0.14
Arthur (H2)	4 July 2014	20.3 (6.5)	2 h	237°	0.42	4 h	0.17
Winter Storm	7 February 2016	17.5 (9.9)	1 h	254°	0.49	6 h	0.28

Matthew (H1)	9 October 2016	20.0 (10.5)	3 h	283°	0.64	11 h	0.28
Florence (H2)	14 September 2018	24.1 (18.3)	13 h	106°	1.12	23 h	0.50
Dorian (H2)	6 September 2019	19.6 (10.6)	3 h	227°	0.41	10 h	0.23

5. Discussion

5.1. Morphological Indicators of Dominant Storm Impact Regimes

Our short-term (i.e., <10 years) synoptic investigation of two openly accessible, remotely sensed datasets reveals dynamic changes to Sugarloaf Island's habitat, shoreline, and morphology between 2014 and 2020, a timeframe that encompasses the impacts of four hurricanes and one strong winter storm on the region. The results of this study highlight the importance of storms as a driver of morphologic change on Sugarloaf Island, similar to other fetch-limited islands documented in the literature [14,15,21]. The locations of four selected topographic profiles distributed across the island are shown in Figure 5. In each of the profiles, blue denotes the topography in 2014, while red is the topography in 2020. Changes in habitat along the profiles and maximum hurricane water levels are also summarized in Figure 5. To contextualize the morphological changes to Sugarloaf Island, refer to the summary of the wind- and water-level observations for the study period, previously shown in Table 3. For reference, coastal terminology usage is consistent with the standards outlined in [78].

Profile 1 (Figure 5A) was extracted from the western spit area of Sugarloaf Island, where substantial changes to the Island's morphology were observed during the study period. Minimal change in habitat type occurred along Profile 1, since this area was predominately sand in 2014 and 2020 (Figures 2A,B and 5A). However, we see a marked change in the location of the spit area with its shoreline location having shifted to the east by approximately 15 m from its original location in 2014. While changes in the horizontal location of the western spit are clearly evident, the feature generally retained its overall shape and appearance, which is consistent with [39]'s conceptual profile translation model. Under nonstorm conditions, the 2014 and 2020 profiles are located within the intertidal zone, both becoming inundated by average MHHW conditions for several hours every day (Table 3). During storm conditions in our study, water levels were, on average, 2 times higher and persisted for 3.5 times longer than average MHHW conditions during nonstorm times (Table 3). The pronounced landward translation of the western spit likely occurs during high-water events that are accompanied by storm waves and is consistent with impacts expected during overwash and inundation regimes on the Sallenger Storm Impact Scale [33–35]. Given the low elevations in this area of Sugarloaf Island, it is highly susceptible to storms where water levels and winds are elevated for prolonged periods, such as Hurricane Florence. During Hurricane Florence, Sugarloaf Island experienced persistent tropical storm-force winds, which coincided with prolonged elevated water levels (Table 3). However, it is also important to consider the orientation of Sugarloaf Island in relation to the average wind direction. For instance, the long axis of Sugarloaf Island is oriented approximately west to east and parallel with the direction of maximum fetch within the Bogue Sound. Storms that produce winds out of the west to southwest, such as Arthur, Winter Storm, Matthew, and Dorian, could enhance wave heights on the western side of Sugarloaf Island given the additional fetch the Island experiences from that direction. It is likely that higher wave energies from the direction of maximum fetch contribute to the observed landward translation despite the lower durations of tropical winds and elevated water levels of the storms when compared to Hurricane Florence (Table 3). However, based on our synoptic dataset, it is uncertain which storm metric is most important for predicting future impacts from specific storms on Sugarloaf Island.

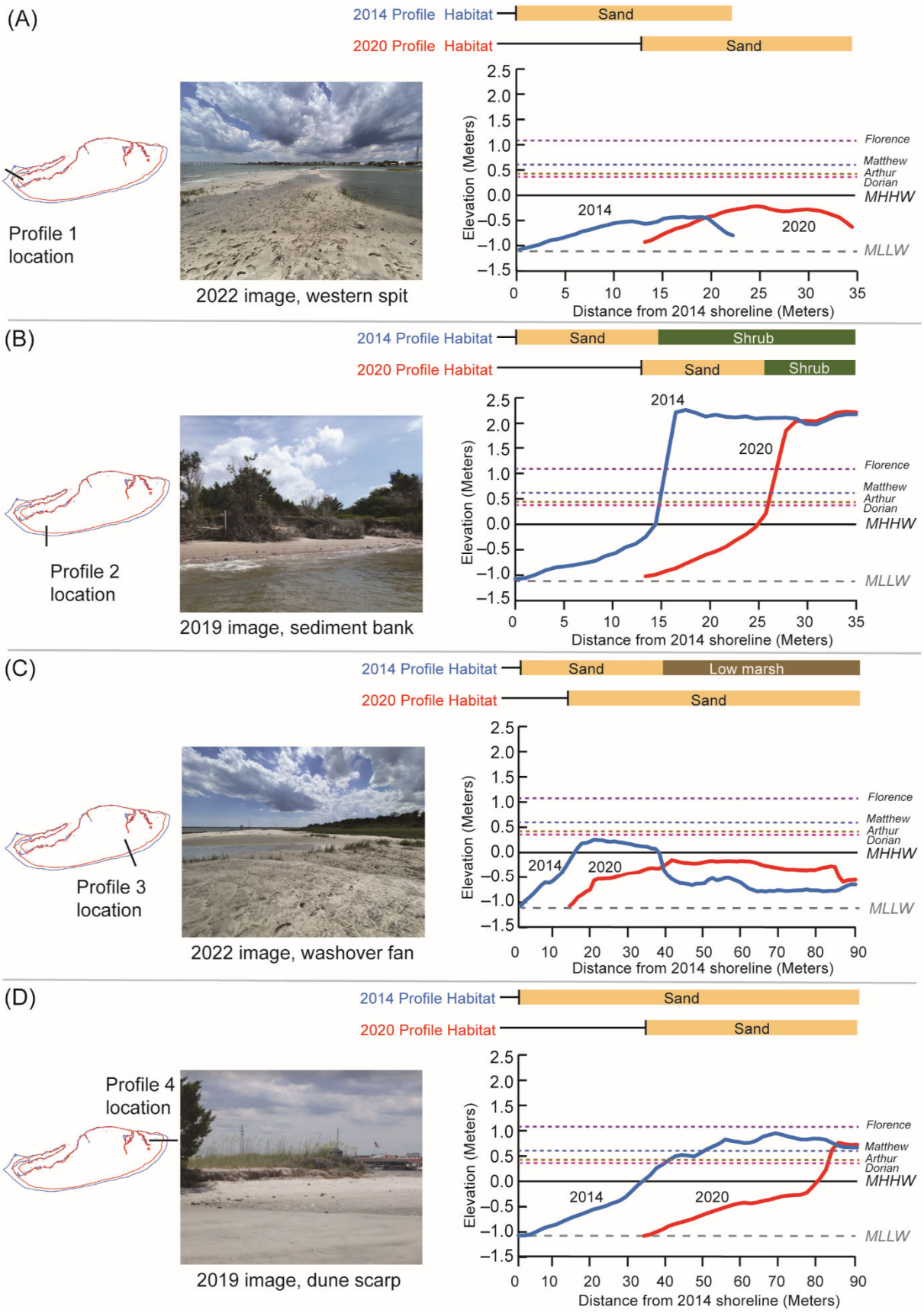

Figure 5. Morphology change is shown at selected profiles where the 2014 shoreline is blue and the 2020 shoreline is red. (**A**) Profile 1 of western spit, (**B**) Profile 2 of sediment bank, (**C**) Profile 3 of beach and foredune flattened into a washover fan, and (**D**) Profile 3 where waves cut back the dune, forming a scarp. The water levels for the four hurricanes are also shown to match the color of their

tracks in Figure 1, as are 2019 images of sediment bank and dune scarp by Niels Lindquist and 2022 images of western spit and washover fan by Matthew Sirianni.

Moving to the east, Profile 2 (Figure 5B) was extracted from the sediment bank of Sugarloaf Island, where substantial erosion occurred. Profile 2 shows a landward shoreline migration of nearly 15 m between 2014 and 2020, which is similar to Profile 1. While a clear change in horizontal position of the sediment bank was observed, the height of the bank remained unchanged between 2014 and 2020. Under nonstorm conditions, the narrow foreshore is situated within the intertidal zone, with the sediment bank toe representing the intersection point of the profile with MHHW. The backshore is characterized by the steep cliff face of the sediment bank that extends approximately 2 m above MHHW. The dominant morphology of this area, a scarp, is indicative of a collision impact regime on the Sallenger Storm Impact Scale. Scarping takes place when the resistive strength of a sediment bank is exceeded by destabilizing forces, such as wave attack, via processes such as sliding, notching, and slumping along failure planes [79–82,]. Considering the height of the sediment bank (Figure 5B) and the water level record (Table 3), it is likely that the sediment bank remains supratidal during storm conditions, which is also consistent with the collision impact regime. Compared to other areas of Sugarloaf Island, the sediment bank is heavily vegetated. Vegetation exerts a strong control on the resistance of the sediment banks to erosion through above- and below-ground biomass [79–82]. As such, the presence of toppled trees and exhumed root systems along the scarp toe are obvious evidence of previous erosion and shoreline retreat events. This response was commonly observed throughout North Carolina's estuaries following Hurricane Florence [83,84], and is likely related to the prolonged and intense storm conditions exerted by Hurricane Florence on Sugarloaf Island (Table 3). Coincidently, foreshore vegetation plays a significant role in dissipating wave energy [85,86]. The presence of foreshore vegetation (albeit dead vegetation in this scenario) along the sediment bank may therefore exert a stabilizing effect and help to prevent future erosion during lower magnitude and shorter duration storms similar to Hurricane Arthur. However, further work is needed to assess how the presence or absence of toe-slope debris contributes to the Island's resiliency and storm response.

The eastern spit shows some of the most striking changes observed in the study, particularly where the washover deposit is present. The extracted profile from this area (i.e., Profile 3 shown in Figure 5C) shows an approximately 15 m shoreline retreat and an overall flattening of the topography between 2014 and 2020. Under nonstorm conditions, the 2014 profile has a roughly 25 m wide supratidal exposure with a maximum height of approximately 0.25 m above MHHW. Immediately beyond the landward extent of the subaerial dune, the topography drops sharply and then smooths out through the rest of the profile. In contrast to the 2014 profile, the 2020 profile is flattened, fully situated within the intertidal zone, and does not have any supratidal exposure. Given the low elevation shown in the 2014 and 2020 profile, this area of Sugarloaf Island is susceptible to overwash and inundation regime impacts considering the persistently elevated water levels during the storm events of this study (Table 3). Unlike the other profiles shown in Figure 5, Profile 3 shows sediment accretion as thick as 0.5 m landward of the 2014 subaerial dune that corresponds with areas that were classified as low marsh in 2014 (Figures 2A,B and 5C). This pattern of foreshore erosion and back barrier marsh deposition is consistent with overwash regime impacts on the Sallenger Storm Impact Scale. It is likely that Hurricane Florence was a major source of overwash, particularly given the parallel orientation of the tropical storm-force winds (Table 3) with the direction of washover deposit growth (Figures 4C and 5C). When coupled with elevated inundation time and inundation magnitude, the higher energy waves generated from tropical storm-force winds were likely sufficient to mobilize the sediment landward. However, it is important to note that given the synoptic nature of our study, individual storm impacts cannot definitively be quantified. While sediment transported to the back barrier marsh contributes to annual marsh

accumulation and can enhance marsh growth [29,87–89], burial of marsh vegetation beyond the optimal depth of 0.05 to 0.1 m has been found to lead to plant mortality [83], which, consequently, impacts island resiliency. Commonly, barrier islands experience breaching and channel incision in response to inundation regime impacts [35]. For instance, the 2014 profile (Figure 5C) shows the presence of a thin supratidal dune that is continuous toward the eastern end of the Island (Figure 4A). In the 2020 profile (Figure 5C), we observe destruction of the dune and the creation of a breach that connects the foreshore with the back barrier marsh via an incised channel (Figure 4B) that was not previously active in 2014 (Figure 4A). Furthermore, it is also notable that the breached area corresponds to a tidal channel seen in the back barrier marsh, suggesting an antecedent control on the position of the breach. The filled channel may extend beneath the barrier to the south and offer less resistance to erosion than the surrounding cohesive marsh peat platforms underlying the foreshore in other areas. A relationship similar to this was noted with respect to the formation of Isabel Inlet on North Carolina's Outer Banks [16].

Extracted from the eastern extent of Sugarloaf Island, Profile 4 (Figure 5D) shows the largest magnitude change in the horizontal location of the shoreline, where roughly 35 m of shoreline migration occurred. The 2014 profile is convex in nature and characterized by a sloped foreshore within the intertidal zone and a backshore with an approximately 60-meter-wide subaerial dune up to 1 m above MHHW at its maximum. Comparatively, the 2020 profile is generally concave in nature and characterized by a wider and more gently sloping foreshore within the intertidal zone and a backshore with a steep scarp and a berm height of approximately 1 m above MHHW. As discussed previously in regard to Profile 2, scarping is an indicator of the collision impact regime on the Sallenger Storm Impact Scale. In contrast to Profile 2, however, Profile 4 does not have extensive vegetation present, as summarized by the horizontal bars above the profile in Figure 5D. The lack of vegetation and its stabilizing influence helps to explain why Profile 4 experienced approximately two times greater horizontal shoreline migration compared to the densely vegetated region of Profile 2 [79–82], since they were both subjected to similar storm conditions (Table 3). Similar to Profile 2, however, the sediment that was eroded from Profile 4 seems to have been lost to transport offshore or longshore, since there is not landward deposition of sediment observed in the profile or in Figure 4C. Without the stabilizing effect of vegetation, this area of the island will likely experience additional scarping during future storm events, shifting the shoreline further inland such as what was observed between 2014 and 2020. Loss of sediment from the Island not only impacts its future persistence, but it also impacts the Port of Morehead City's navigational channels surrounding the Island, since the sand is known to be infilling the channel on the Island's eastern end.

5.2. Implications for Future Restoration Monitoring

Due to growing concern over Sugarloaf Island's continued erosional issues, plans are being made to increase the resiliency of Morehead City's downtown waterfront by enhancing Sugarloaf Island's capacity to (1) mitigate disturbances such as hurricanes and (2) return to a predisturbance state. Commonly, structural hardening of the shoreline through bulkheads, seawalls, and revetments is one way in which coastal communities have attempted to address erosional issues [90]. However, these hardened structures can bring about a number of negative side-effects such as loss of biodiversity, erosion and scouring, reduced storm protection, and loss of ecosystem services [91–95]. Alternatively, nature-based infrastructure solutions, such as living shorelines, have recently gained attention as a method to increase coastal resiliency while limiting negative repercussions [92–95]. Living shorelines work by harnessing the adaptive capacity of natural habitats, such as salt marshes and oyster reefs, in combination with low-lying engineered structures, such as sills and breakwaters, to stabilize the shoreline and restore critical habitat and ecosystem services [92–95]. Since each restoration technique has its pros and cons, the Sugarloaf Island project design aims to employ a hybrid approach that combines nature-based solutions and engineered structures to enhance the Island's resiliency. This hybrid approach

consists of several living shoreline restoration approaches and includes offshore hollow Wave Attenuation Devices (WADs), seagrass planting, oyster reef installation, and upland dune enhancement. WADs may be able to reduce wave heights and stabilize the shoreline position and volume of sand on the beach during storms, but this will depend on the Island's coastal processes and underlying geology [96]. Seagrasses can provide additional erosion control, habitat for economically important aquatic species, and carbon sequestration [97]; however, seagrass beds cannot be installed until sediment has gathered landward of the WAD and wave-sheltered conditions are present. Oyster reefs complement seagrass beds and provide habitat, water filtration, coastal stabilization, and fisheries, which can enhance recreation, although this can be highly variable by location [98]. Upland dune enhancement through the planting of appropriate plants, such as *Spartina patens*, can help to stabilize existing dune features, adding to the sediment's cohesiveness via above-ground and below-ground biomass and trapping aeolian transported sediment. Assessment of similar designs demonstrates that marsh vegetation is established within three to eight years, and sediment accretion and organic matter accumulation occur at rates similar to or greater than natural fringing marsh [93,99]. However, the success of these projects will vary regionally and are based on specific design parameters [100]. Considering that sediment from Sugarloaf Island is infilling the Port of Morehead City's navigational channels, dredge spoils are a potential sediment source for new dune and beach creation; however, periodic replenishment of the sediment will likely be needed [101]. Ideally, all of these approaches will work in conjunction with one another to stabilize the island while also continuing to provide public recreational access to the Island for boating, fishing, and beach-going. Short- and long-term monitoring of Sugarloaf Island is another critical future component of the project since there is a distinctive need to understand the efficacy of living shorelines and other restoration devices at different spatial and temporal scales to improve coastal resiliency [94,95]. With the rapid advancement of small Unoccupied Aircraft Systems (sUAS) (e.g., [102]), on-demand remote sensing devices are available for high-resolution, real-time monitoring pre- and poststorms and long-term resiliency assessments. Given that aerial imagery has a limited ability to measure bathymetry, future work should consider coupling sUAS imagery data with nearshore bathymetric data, or the use of a sUAS equipped with a topobathymetric LiDAR payload, for a more holistic understanding of the coastal geomorphology.

5.3. Study Limitations

The most glaring limitation of this study is its synoptic nature, in that we are only able to infer the cumulative impact of storms rather than assess specific storm event impacts. For example, our dataset shows erosion over the six-year period of the study, which we inferred to be related to episodic occurrence of hurricanes based on an interpretation of the predominant morphological features on the Island. However, studies such as [21] used sUAS imagery and higher-frequency surveys to capture a fetch-limited island response to individual storms and identify a pattern of poststorm recovery that contradicts the standard evolutionary model [15]. Our study was unable to determine if Sugarloaf Island experienced any recovery period following the storms that impacted the area during the study; thus, it is unclear if the Island conforms to the standard evolutionary model for fetch-limited islands [15] or contradicts the model [21]. Yet, even with higher-frequency surveys, repeated storms in quick succession can prevent or potentially mask a recovery stage, which could thus lead to the misclassification of the Island's poststorm behavior.

While LiDAR and aerial imagery are critical tools for monitoring coastal change, it is important to understand their associated limitations. For example, timing available satellite and/or aircraft coverage to coincide with pre-/poststorm comparisons can be difficult, and factors such as weather conditions, sun angle, and water levels can negatively impact the quality or comparability of the collected datasets [103]. Moreover, the datasets' spatial resolution and geolocation error are important considerations, as changes in location and

elevation below that error threshold cannot be differentiated from noise in the data [21]. While the availability of openly accessible and reliable remotely sensed data is a great benefit, it comes at a cost, because ground truth data for certain locations are often not collected simultaneously. The logistics of collecting ground truth data simultaneously with state or federal government survey campaigns can be complex. For this study, it would have been best to collect RTK-GNSS data with corresponding attributes of latitude, longitude, elevation, and vegetation species at hundreds of locations spread throughout the Island. Since the Island is experiencing rapid change, it would be best to collect the data for both dates being monitored, which can be labor intensive and expensive, since the Island is only accessible by boat. This type of data could then be used to train and validate a machine learning or deep learning model to better classify habitat and coastal landforms [104]. Another use of this data would be as a correction factor for the LiDAR DEMs, particularly in the marsh areas where LiDAR may not penetrate the vegetation and thus overestimate the marsh surface [105]. Moreover, ground truth data would also allow for each DEM's error to be analyzed spatially when calculating the volume of sediment deposition and erosion on the Island [74]. This issue of collecting ground truth data simultaneously can be addressed with sUAS survey campaigns, which involves experienced scientific pilots and data processing and analysis workflows [106].

In addition to the DEM error, future work should consider the transformation errors when defining the minimum critical threshold for determining vertical changes. In this study, we used the DEM's Linear Error (LE) at a 95% confidence interval (RMSE × 1.96 = LE) [76] to define the minimum critical threshold to estimate erosion and deposition volumes. Our estimates are likely overestimated because they do not incorporate the uncertainty in datum transformations. It is best to consider the DEM and transformation error when defining the minimum critical threshold.

6. Conclusions

In this study, we used openly accessible topobathymetric LiDAR and aerial imagery to quantify synoptic changes to Sugarloaf Island's habitat, shoreline, and morphology in response to storms between 2014 and 2020. Our workflow uses several proven data processing and analysis techniques by combining OBIA to segment the images into homogeneous vegetation patches rather than pixels, machine learning to classify the landscape patches into habitat types, and raster algebra to calculate areas of sediment erosion and deposition. Our results highlight the overall impact of recent storms on the Island and demonstrate that the Island's current morphology is a legacy of cumulative storm impacts, which is consistent with other previous studies. In summary, Sugarloaf Island lost approximately 1.7 ha of area and 9800 m^3 of sediment during the study period. Although this study is limited by its lack of individual storm impact quantification, it suggests that if the current trend in storms continues, Sugarloaf Island may not recover naturally and may therefore be susceptible to further inundation or rapid transgression and erosion. Due to growing concern over Sugarloaf Island's dynamic erosion problem, a multidisciplinary coastal governance project that combines efforts from private citizens, governmental and nongovernmental organizations, and academia was brought together to design and implement a shoreline stabilization project for future implementation. In order to manage and monitor the project's success, the authors suggest that future work should implement the use of sUAS and RTK-GNSS in seasonal and/or annual surveys.

Author Contributions: Conceptualization, H.S., M.J.S., D.J.M., N.L.L., L.M.V.-W., M.M., B.H., B.R., C.C., M.M.P. and C.H.; Methodology, H.S.; formal analysis, H.S.; writing—original draft preparation, H.S. and M.J.S.; writing—review and editing, H.S., M.J.S. and D.J.M.; All authors have read and agreed to the published version of the manuscript.

Funding: This research received no external funding.

Institutional Review Board Statement: Not applicable.

Informed Consent Statement: Not applicable.

Data Availability Statement: LiDAR and aerial imagery data are publicly available at: https://coast.noaa.gov/dataviewer/#/; accessed on 25 October 2022). Wind and water level data are publicly available at: https://tidesandcurrents.noaa.gov/; accessed on 25 October 2022).

Acknowledgments: We thank the town of Morehead City, N.C., for its cooperation and support. We thank the editors and four anonymous reviewers for their role in improving the manuscript through peer review.

Conflicts of Interest: The authors declare no conflict of interest.

References

1. Stutz, M.L.; Pilkey, O.H. Open-ocean barrier islands: Global influence of climatic, oceanographic, and depositional settings. *J. Coast. Res.* **2011**, *27*, 207–222.
2. De Beaumont, L.E. *Lecons de Geologie Practique*; Bertrand, S.L.P., Ed.; Biblioteca Santa Scholastica: Subiaco, Italy, 1845; pp 221–252.
3. Gilbert, G.K. *The Topographic Features of Lake Shores*; 5th Annual Report; US Government Printing Office: Washington, DC, USA, 1885; pp 69–123.
4. Johnson, D.W. *Shore Processes and Shoreline Development*; Hafner Publishing Company: New York, NY, USA, 1919.
5. Hoyt, J.H. Barrier island formation. *Geol. Soc. Amer. Bull.* **1967**, *78*, 1125–1135.
6. Dolan, R. Barrier Dune system along the Outer Banks of North Carolina: A reappraisal. *Science* **1972**, *176*, 280–288.
7. Godfrey, P.J.; Godfrey, M.M. *Barrier Island Ecology of Cape Lookout National Seashore and Vicinity, North Carolina*; National Park Service Scientific Monograph Series, No. 9; National Park Service: Washington, DC, USA, 1976; p. 160.
8. Oertel, G.F. The Barrier Island System. *Mar. Geol.* **1985**, *63*, 1–18.
9. Davis, R.A. *Geology of Holocene Barrier Island Systems*; Springer-Verlag: New York, NY, USA, 1994; p. 464.
10. Hayes, M.O. Barrier island morphology as a function of tidal and wave regime. In *Barrier Islands: From the Gulf of St. Lawrence to the Gulf of Mexico*; Leatherman, S.P., Ed.; Academic Press: New York, NY, USA, 1979; pp. 1–29.
11. Hayes, M.O. The Georgia Bight barrier system. In *Geology of Holocene Barrier Island Systems*; Davis, R.A., Jr., Ed.; Springer: Berlin, Germany, 1994; pp. 233–304.
12. Riggs, S.R.; Cleary, W.J.; Snyder, S.W. Influence of inherited geologic framework on barrier shoreface morphology and dynamics. *Mar. Geol.* **1995**, *126*, 213–234.
13. Pilkey, O.H. *Celebration of the World's Barrier Islands*; Columbia University Press: New York, NY, USA, 2003; p. 400.
14. Lewis, D.A.; Cooper, J.A.G.; Pilkey, O.H. Fetch-limited barrier islands of Chesapeake Bay and Delaware Bay USA. *Southeast. Geol.* **2005**, *44*, 1–17.
15. Pilkey, O.H.; Cooper, J.A.G.; Lewis, D.A. Global distribution and geomorphology of fetch-limited barrier islands. *J. Coast. Res.* **2009**, *254*, 819–837. https://doi.org/10.2112/08-1023.1.
16. Mallinson, D.J.; Smith, C.W.; Culver, S.J.; Riggs, S.R.; Ames, D.V. Geological characteristics and spatial distribution of paleo-inlet channels beneath the Outer Banks barrier islands, North Carolina, USA. *Estuar. Coast Shelf Sci.* **2010**, *88*, 175–189.
17. Mallinson, D.J.; Smith, C.W.; Mahan, S.; Culver, S.J.; McDowell, K. Barrier island processes and response to late Holocene climate patterns: Outer Banks barrier islands, North Carolina, USA. *Quat. Res.* **2011**, *76*, 46–57.
18. Fitzgerald, D.M.; Georgiou, I.; Hein, C.; Hughes, Z.; Kulp, M.; Miner, M. Runaway barrier island transgression concept: Global case studies. In *Barrier Dynamics and the Impact of Climate Change on Barrier Evolution*; Moore, L., Murray, B., Ed.; Springer: New York, NY, USA, 2018.
19. Cooper, J.A.G.; Lewis, D.A.; Pilkey, O.H. Fetch-limited barrier islands: Overlooked coastal landforms. *GSA Today* **2007**, *17*, 4–9. https://doi.org/10.1130/GSAT01703A.1.
20. Neumann, B.; Vafeidis, A.T.; Zimmermann, J.; Nicholls, R.J. Future coastal population growth and exposure to sea-level rise and coastal flooding–a global assessment. *PLoS ONE* **2015**, *10*, e0118571. https://doi.org/10.1371/journal.pone.0118571.
21. Seymour, A.C.; Ridge, J.T.; Newton ERodriguez, A.B.; Johnston, D.W. Geomorphic response of inlet barrier islands to storms. *Geomorphology* **2019**, *339*, 127–140.
22. Feagin, R.A.; Smith, W.K.; Psuty, N.P.; Young, D.R.; Martinez, M.L.; Carter, G.A.; LUCAS, K.L.; Gibeaut, J.C.; Gemma, J.N.; Koske, R.E. Barrier islands: Coupling anthropogenic stability with ecological sustainability. *J. Coast. Res.* **2010**, *26*, 987–992.
23. Anderson, C.P.; Carter, G.A.; Funderburk, W.R. The Use of Aerial RGB Imagery and LIDAR in Comparing Ecological Habitats and Geomorphic Features on a Natural versus Man-Made Barrier Island. *Remote Sens.* **2016**, *8*, 602.
24. Valle-Levinson, A.; Dutton, A.; Martin, J.B. Spatial and temporal variability of sea level rise hot spots over the eastern United States. *Geophys. Res. Lett.* **2017**, *44*, 7876–7882. https://doi.org/10.1002/2017GL073926.
25. Paerl, H.W.; Hall, N.S.; Hounshell, A.G.; Luettich, R.A., Jr.; Rossingnol, K.L.; Osburn, C.L.; Bales, J. Recent increase in catastrophic tropical cyclone flooding in coastal North Carolina, USA: Long-term observations suggest a regime shift. *Sci. Rep.* **2019**, *9*, 10620. https://doi.org/10.1038/s41598-019-46928-9.
26. Mariotti, G.; Hein, C.J. Lag in response of coastal barrier-island retreat to sea-level rise. *Nat. Geosci.* **2022**, *15*, 633–638. https://doi.org/10.1038/s41561-022-00980-9.

27. Jackson, N.L. Wind and waves: Influence of local and non-local waves on mesoscale beach behaviour in estuarine environments. *Ann. Assoc. Am. Geogr.* **1995**, *85*, 21–37.
28. Jackson, N.L.; Nordstrom, K.F.; Eliot, I.; Masselink, G. "Low energy" sandy beaches in marine and estuarine environments: A review. *Geomorphology* **2002**, *48*, 147–162. https://doi.org/10.1016/s0169-555x(02)00179-4.
29. Baustian, J.J.; Mendelssohn, I.A. Hurricane-induced sedimentation improves marsh resilience and vegetation vigor under high rates of relative sea level rise. *Wetlands* **2015**, *35*, 795–802. https://doi.org/10.1007/s13157-015-0670-2.
30. Nordstrom, K.F. Cyclic and seasonal beach response: A comparison of oceanside and bayside beaches. *Phys. Geogr.* **1980**, *1*, 177–196. https://doi.org/10.1080/ 02723646.1980.10642199.
31. Suanez, S.; Cariolet, J.M.; Cancouët, R.; Ardhuin, F.; Delacourt, C. Dune recovery after storm erosion on a high-energy beach: Vougot Beach, Brittany (France). *Geomorphology* **2012**, *139–140*, 16–33. https://doi.org/10.1016/j.geomorph.2011.10.014.
32. Houser, C.; Wernette, P.; Rentschlar, E.; Jones, H.; Hammond, B.; Trimble, S. Poststorm beach and dune recovery: Implications for barrier island resilience. *Geomorphology* **2015**, *234*, 54–63. https://doi.org/10.1016/j.geomorph.2014.12.044.
33. Sallenger, A.H. Storm impact scale for barrier islands. *J. Coast. Res.* **2000**, *16*, 890–895.
34. Wang, P.; Briggs, T. Storm-Induced Morphology Changes along Barrier Islands and Poststorm Recovery. In *Coastal and Marine Hazards, Risks, and Disasters*; Shroder, J.F., Ellis, J.T., Sherman, D.J., Eds.; Elsevier: Amsterdam, The Netherlands, 2015; pp. 271–306.
35. Morton, R.A. Factors controlling storm impacts on coastal barriers and beaches-a preliminary basis for near real-time forecasting. *J. Coast. Res.* **2002**, *18*, 486–501.
36. Stockdon, H.F.; Sallenger, A.H., Jr.; Holman, R.A.; Howd, P.A. A simple model for the spatially-variable coastal response to hurricanes. *Mar. Geol.* **2007**, *238*, 1–20.
37. Liu, H.X. Shoreline mapping and coastal change studies using remote sensing imagery and LIDAR data. In *Remote Sensing and Geospatial Technologies for Coastal Ecosystem Assessment and Management*; Yang, X., Ed.; Springer: New York, NY, USA, 2009; pp. 297–322.
38. Glennie, C.L.; Carter, W.E.; Shrestha, R.L.; Dietrich, W.E. Geodetic imaging with airborne LiDAR: The Earth's surface revealed. *Rep. Prog. Phys.* **2013**, *76*, 086801.
39. Smith, C.G.; Culver, S.J.; Riggs, S.R.; Ames, D.; Corbett, D.R.; Mallinson, D. Geospatial analysis of barrier island width of two segments of the Outer Banks, North Carolina, USA: Anthropogenic curtailment of natural self-sustaining processes. *J. Coast. Res.* **2008**, *24*, 70–83.
40. Juel, A.; Groom, G.B.; Svenning, J.C.; Ejrnaes, R. Spatial application of Random Forest models for fine-scale coastal vegetation classification using object based analysis of aerial orthophoto and DEM data. *Int. J. Appl. Eart.h Obs. Geoinf.* **2015**, *42*, 106–114.
41. McCarthy, M.J.; Colna, K.E.; El-Mezayen, M.M.; Laureano-Rosario, A.E.; Méndez-Lázaro, P.; Otis, D.B.; Toro-Farmer, G.; Vega-Rodriguez, M.; Muller-Karger, F.E. Satellite Remote Sensing for Coastal Management: A Review of Successful Applications. *Environ. Manag.* **2017**, *60*, 323–339. https://doi.org/10.1007/s00267-017-0880-x.
42. Crawford, T. North Carolina's Final Coastal Frontier: Land Cover Change in the Inner Banks, 1996–2001. *N. C. Geog.* **2007**, *15*, 37–52.
43. Gharagozlou, A.; Dietrich, J.C.; Karanci, A.; Luettich, R.A.; Overton, M.F. Storm-driven erosion and inundation of barrier islands from dune-to region-scales. *Coast. Eng.* **2020**, *158*, 103674.
44. United States Coast and Geodetic Survey. *Coast Chart No. 147, Core Sound to Bogue Inlet Including Cape Lookout, North Carolina*; United States Coast and Geodetic Survey: Washington, DC, USA, 1888.
45. United States Coast and Geodetic Survey. *Coast Chart No. 147, Core Sound to Bogue Inlet Including Cape Lookout, North Carolina*; United States Coast and Geodetic Survey: Washington, DC, USA, 1913.
46. Angley, F.W. *Historical overview of Beaufort Inlet, Cape Lookout Area of North Carolina*; North Carolina Department of Natural and Cultural Resources: Raleigh, NC, USA, 1982. Available online: https://digital.ncdcr.gov/digital/collection/p16062coll6/id/10345/ (accessed on 25 October 2022).
47. Evans, J.P. *Plant Succession and Stabilization of Dredge Spoil Habitats in the Rachel Carson National Estuarine Research Reserve*; NC. National Oceanic and Atmospheric Administration Technical Memorandum: Washington, DC, USA, 1988.
48. United States Environmental Protection Agency; United States Army Corps of Engineers. *Morehead City Ocean Dredged Material Disposal Site (ODMDS) Site Management and Monitoring Plan*; United States Environmental Protection Agency: Washington, DC, USA; Fort Belvoir, VA, USA, 2020.
49. Google Earth Engine Timelapse. Available online: https://earthengine.google.com/timelapse/#v=34.716758,-76.710594,11.973,latLng&t=3.23 (accessed on 15 October 2018).
50. Suchrow, S.; Jensen, K. Plant Species Responses to an Elevational Gradient in German North Sea Salt Marshes. *Wetlands* **2010**, *30*, 735–746.
51. Zhang, C.; Denka, S.; Mishra, D.R. Mapping Freshwater Marsh Species in the Wetlands of Lake Okeechobee using Very High-resolution Aerial Photography and Lidar Data. *Int. J. Remote Sens.* **2018**, *39*, 5600–5618.
52. Office for Coastal Management. 2022: 2014 NOAA Post-Sandy Topobathymetric LiDAR: Void DEMs South Carolina to New York. Available online: https://www.fisheries.noaa.gov/inport/item/48367 (accessed on 25 October 2022).
53. National Geodetic Survey. 2022a: 2019–2020 NOAA NGS Topobathy Lidar DEM: Coastal VA, NC, SC. Available online: https://www.fisheries.noaa.gov/inport/item/66714 (accessed on 25 October 2022).

54. National Geodetic Survey. 2022b: 2014 NOAA Ortho-rectified Mosaic of Hurricane Sandy Coastal Impact Area. Available online: https://www.fisheries.noaa.gov/inport/item/48588 (accessed on 25 October 2022).
55. National Geodetic Survey. 2022c: 2020 NOAA NGS Ortho-rectified Color Mosaic Hurricane Florence: NC, SC, and VA. Available online: https://www.fisheries.noaa.gov/inport/item/66699 (accessed on 25 October 2022).
56. Boak, E.H.; Turner, I.L. Shoreline Definition and Detection: A Review. *J. Coast. Res.* **2005**, *21*, 688–703.
57. Nyandwi, N. Reassessment of the nature of beach erosion north of Dar es Salaam, Tanzania. Marine SCIENCE development in Tanzania and Eastern Africa. In Proceedings of the 20th Anniversary Conference on Advances in Marine Science in Tanzania, Zanzibar, Tanzania, 28 June–1 July 1999; Richmond, M.D., Francis, J., Eds.; IMS/WIOMSA: Zanzibar, Tanzania; pp. 107–120.
58. Nayak, S.R. Use of satellite data in coastal mapping. *In. Cart.* **2002**, *22*, 1.
59. Pugh, D. *Changing Sea Levels: Effects of Tides, Weather and Climate*; Cambridge University Press: Cambridge, UK, 2004; p. 280.
60. Shaghude, Y.W.; Wannäs, K.O.; Lunden, B. Assessment of shoreline changes in the western side of Zanzibar channel using satellite remote sensing. *Int. J. Remote Sens.* **2003**, *24*, 4955–4969.
61. Shaghude, Y.W. Coastal Impacts of Water Abstraction and Impoundment in Africa: The Case of Rufiji River. Final Report Submitted to START; OceanDocs: E-Repository of Ocean Publications; 2004. Available online: https://aquadocs.org/handle/1834/187 (accessed on 25 October 2022).
62. Kumar, D.A.; Venkatanarayana, M.; Murthy, V.S.S. Object-Based Image Analysis. In *Encyclopedia of Mathematical Geosciences*; Daya Sagar, B., Cheng, Q., McKinley, J., Agterberg, F., Eds.; Encyclopedia of Earth Sciences Series; Springer: Cham, Switzerland, 2021. https://doi.org/10.1007/978-3-030-26050-7_229-1.
63. Breiman, L. Random Forests. *Mach. Learn.* **2001**, *45*, 5–32.
64. Belgiu, M.; Draguţ, L. Random forest in remote sensing: A review of applications and future directions. *ISPRS J. Photogram. Remote Sens.* **2016**, *114*, 24–31.
65. Zhang, C.; Mishra, D.R.; Pennings, S. Mapping Salt Marsh Soil Properties Using Imaging Spectroscopy. *ISPRS J. Photogram. Remote Sens.* **2019**, *148*, 221–234.
66. Comaniciu, D. Mean Shift: A Robust Approach Toward Feature Extraction Space Analysis. *IEEE PAMI* **2022**, *24*, 603–619.
67. Gens, R. Remote sensing of coastlines: Detection, extraction and monitoring. *Int. J. Remote Sens.* **2010**, *31*, 1819–1836. https://doi.org/10.1080/01431160902926673.
68. Fisher, J.S.; Overton, M.F. Interpretation of shoreline position from aerial photographs. In Proceedings of the 24th International Conference on Coastal Engineering, Kobe, Japan, 23–28 October 1994.
69. Woolard, J.W.; Aslaksen, M.; Longenecker, J.L.T.; Ryerson, A. Shoreline mapping from airborne lidar in Shilshole Bay, Washington. In Proceedings of the National Oceanic and Atmospheric Administration (NOAA) National Ocean Service (NOS), US Hydrographic Conference, Washington, DC, USA, 3 February 2003.
70. Office of Coast Survey. 2014. Datums and transformations. Available online: http://www. nauticalcharts.noaa.gov/csdl/ learn datum.html (accessed on 25 October 2022).
71. Cowart, L.; Walsh, J.P.; Corbett, D.R. Analyzing estuarine shoreline change: A case study of cedar island, North Carolina. *J. Coast. Res.* **2010**, *26*, 817–830.
72. Currin, C.; Davis, J.; Cowart Baron, L.; Malhotra, A.; Fonseca, M. Shoreline change in the New River Estuary, North Carolina: Rates and consequences. *J. Coast. Res.* **2015**, *31*, 1069–1077.
73. Lane, S.N.; Chandler, J.H.; Richards, K.S. Developments in monitoring and modeling small-scale river bed topography. *Earth Surf. Process. Landf.* **1994**, *19*, 349–368. https://doi.org/10.1002/ esp.3290190406.
74. Wheaton, J.M.; Brasington, J.; Darby, S.E.; Sear, D.A. Accounting for uncertainty in DEMs from repeat topographic surveys: Improved sediment budgets. *Earth Surf. Process. Landf.* **2010**, *35*, 136–156. https://doi.org/10.1002/esp.1886.
75. James, M.R.; Robson, S.; Smith, M.W. 3-D uncertainty-based topographic change detection with structure-from-motion photogrammetry: Precision maps for ground control and directly georeferenced surveys. *Earth Surf. Process. Landf.* **2017**, *42*, 1769-1788.
76. Federal Geographic Data Committee (FGDC). *Geospatial Positioning Accuracy Standards, Part 3: National Standard for Spatial Data Accuracy*; US Geological Survey Report no. FGDC-STD-007.3-1998; Federal Geographic Data Committee Secretariat, Reston, VA, USA, 1998.
77. Anderson, J.R.; Hardy, E.E.; Roach, J.T.; Witmer, R.E. *A Land Use and Land Cover Classification System for Use with Remote Sensor Data*; Geological Survey Professional Paper No. 964, U.S.; Government Printing Office: Washington, DC, USA, 1976; p. 28.
78. USACE. *Coastal Engineering Manual*; Report No 110-2-1100; US Army Corps of Engineers: Washington, DC, USA, 2012. Available online: https://www.publications.usace.army.mil/USACE-Publications/Engineer-Manuals/u43544q/636F617374616C20656E67696E656572696E67206D616E75616C/ (accessed on 25 October 2022).
79. Barbier, E.B.; Koch, E.W.; Silliman, B.R.; Hacker, S.D.; Wolanski, E.; Primavera, J.; Reed, D.J. Coastal ecosystem-based management with nonlinear ecological functions and values. *Science* **2008**, *319*, 321–323.
80. Tiggeloven, T.; de Moel, H.; van Zelst, V.T.; van Wesenbeeck, B.K.; Winsemius, H.C.; Eilander, D.; Ward, P.J. The benefits of coastal adaptation through conservation of foreshore vegetation. *J. Flood Risk Manag.* **2022**, *15*, e12790.
81. Phillips, J.D. Geomorphic impacts of Hurricane Florence on the lower Neuse River: Portents and particulars. *Geomorphology* **2022**, *397*, 108026.
82. Davidson, S.G.; Hesp, P.A.; Silva, G.M.D. Controls on dune scarping. *Prog. Phys. Geogr. Ear. Env.* **2020**, *44*, 923–947.

83. Walters, D.C.; Kirwan, M.L. Optimal hurricane overwash thickness for maximizing marsh resilience to sea level rise. *Ecol. Evol.* **2016**, *6*, 2948–2956. https://doi.org/10.1002/ece3.2024.
84. Moore, L.J.; Patsch, K.; List, J.H.; Williams, S.J. The potential for sea-level-rise-induced barrier island loss: Insights from the Chandeleur Islands, Louisiana, USA. *Mar. Geol.* **2014**, *355*, 244–259.
85. Sallenger, A.; Wright, W.; Lillycrop, J.; Howd, P.; Stockdon, H.; Guy, K.K.; Morgan, K. *Extreme Changes to Barrier Islands along the Central Gulf of Mexico Coast during Hurricane Katrina*; No. 1306-5C; US Geological Survey: Reston, VA, USA, 2007; pp. 113–118.
86. Dingler, J.R.; Reiss, T.E. Beach erosion on Trinity Island, Louisiana caused by Hurricane Andrew. *J. Coast. Res.* **1995**, *21*, 254–264.
87. Hein, C.J.; Fenster, M.S.; Gedan, K.B.; Tabar, J.R.; Hein, E.A.; DeMunda, T. Leveraging the Interdependencies Between Barrier Islands and Backbarrier Saltmarshes to Enhance Resilience to Sea-Level Rise. *Front. Mar. Sci.* **2021**, *8*, 721904. https://doi.org/10.3389/fmars.2021.721904.
88. Cahoon, D.R.; Reed, D.; Day, J.W.; Steyer, D.; Boumans, R.M.; Lynch, C.J.; McNally, D.; Latif, N. The influence of Hurricane Andrew on sediment distribution in Louisiana coastal marshes. *J. Coast. Res.* **1995**, *21*, 280–294.
89. Tweel, A.W.; Turner, R.E. Contribution of tropical cyclones to the sediment budget for coastal wetlands in Louisiana. USA. *Landsc. Ecol.* **2014**, *29*, 1083–1094.
90. Dugan, J.E.; Airoldi, L.; Chapman, M.G.; Walker, S.J.; Schlacher, T.; Wolanski, E.; McLusky, D. Estuarine and coastal structures: Environmental effects a focus on shore and nearshore structures. *Treat. Estuar. Coast. Sci.* **2011**, *8*, 17–41.
91. Riggs, S.R. *Report No.: UNC-SG-01-11*; Shoreline Erosion in North Carolina Estuaries. North Carolina Sea Grant Program Publication: Raleigh, NC, USA, 2001.
92. Gittman, R.K.; Popowich, A.M.; Bruno, J.F.; Peterson, C.H. Marshes with and without sills protect estuarine shorelines from erosion better than bulkheads during a category 1 hurricane. *Ocean Coast. Manag.* **2014**, *102*, 94–102. https://doi.org/10.1016/j.ocecoaman.2014. 09.016.
93. Gittman, R.K.; Peterson, C.H.; Currin, C.A.; Fodrie, F.J.; Piehler, M.F.; Bruno, J.F. Living shorelines can enhance the nursery role of threatened estuarine habitats. *Ec. Soc. Am.* **2016**, *26*, 249–263.
94. Gittman, R.K.; Smith, C.; Neylan, I.; Grabowski, J. Ecological consequences of shoreline hardening: A meta-analysis. *BioScience* **2016**, *66*, 760–773.
95. Polk, M.A.; Gittman, R.K.; Smith, C.S.; Eulie, D.O. Coastal resilience surges as living shorelines reduce lateral erosion of salt marshes. *Integr. Environ. Assess. Manag.* **2022**, *18*, 82–98.
96. Stauble, D.K.; Tabar, J.R. The use of submerged narrow-crested breakwaters for shoreline erosion control. *J. Coast. Res.* **2003**, *19*, 684–722.
97. Barbier, E.B.; Hacker, S.D.; Kennedy, C.; Koch, E.W.; Stier, A.C.; Silliman, B.R. The value of estuarine and coastal ecosystem services. *Ecol. Monogr.* **2011**, *81*, 169–193.
98. Grabowski, J.H.; Brumbaugh, R.D.; Conrad, R.F.; Keeler, A.G.; Opaluch, J.J.; Peterson, C.H.; Piehler, M.; Powers, S.; Smyth, A.R. Economic valuation of ecosystem services provided by oyster reefs. *BioScince* **2012**, *81*, 169–193.
99. Currin, C.A. Chapter 30—Living Shorelines for Coastal Resilience. In *Coastal Wetlands*; Perillo, G.M.E., Wolanski, E., Cahoon, D.R., Hopkinson, C.S., Eds.; Elsevier: Amsterdam, The Netherlands, 2019; pp. 1023–1053, ISBN 9780444638939. https://doi.org/10.1016/B978-0-444-63893-9.00030-7.
100. Bilkovic, D.M.; Mitchell, M.; Mason, P.; Duhring, K. The role of living shorelines as estuarine habitat conservation strategies. *Coast. Manag.* **2016**, *44*, 161–174.
101. Duhring, K. *Overview of Living Shoreline Design Options for Erosion Protection on Tidal Shorelines*; VIMS Books and Book Chapters 123; Chesapeake Research Consortium: Edgewater, MD, USA, 2008. Available online: https://scholarworks.wm.edu/vimsbooks/126 (accessed on 25 October 2022).
102. Tmušic, G.; Salvator, M.; Helge, A.; James, M.R.; Goncalves, G.; Ben-Dor, E.; Brook, A.; Polinova, M.; Arranz, J.J.; Mészáros, J.; et al. Current practices in UAS-based environmental monitoring. *Remote Sens.* **2020**, *12*, 1001.
103. Tysiac, P. Bringing bathymetry LiDAR to coastal zone assessment: A case study in the Southern Baltic. *Remote Sens.* **2020**, *12*, 3740.
104. Lamba, A.; Cassey, P.; Segaran, R.R.; Lian, P. Deep learning for environmental conservation. *Curr. Biol.* **2019**, *29*, R977–R982.
105. Cooper, H.; Zhang, C.; Davis, S.; Troxler, T. Object-based correction of LiDAR DEMs using RTK-GPS data and machine learning modeling in the Coastal Everglades. *Env. Mod. Soft.* **2019**, *112*, 179–191. https://doi.org/10.1016/j.envsoft.2018.11.003.
106. Guan, S.; Sirianni, H.; Wang, G.; Zhu, Z. sUAS monitoring of coastal environments: A review of best practices from field to lab. *Drones* **2022**, *6*, 142; https://doi.org/10.3390/drones6060142.